

# Enhanced Piezoelectric Performance of Electrospun PVDF-TrFE by Polydopamine-Assisted Attachment of ZnO Nanowires for Impact Force Sensing

Michael Chung, Francisco J. Diaz Sanchez, Jean Schoeller, Rolf Stämpfli, René M. Rossi, and Norbert Radacsi\*

In this work, piezoelectric PVDF-TrFE electrospun fibers (EFs) were fabricated using a high-throughput nozzle-free electrospinning process. Zinc oxide (ZnO) nanoparticles were robustly anchored to the PVDF-TrFE EFs, assisted by a self-polymerized polydopamine (PDA) layer, and subsequently grown into ZnO nanowires (NWs) using a low-temperature hydrothermal growth method. The EF mats were investigated for active impact force transduction and the piezoelectric voltage outputs of different combinations of PVDF-TrFE and ZnO nanomaterials were compared using two different impact force testing setups. The horizontal impact force test saw an increase in force sensitivity by a factor of 2.5 for the nanowires compared to the unmodified PVDF-TrFE EFs. Similarly, vertical drop impact testing demonstrated a 5.8-fold increase in sensitivity with a linear response ( $R^2 = 0.986$ ) for a large range of impact forces up to 970 N. The EFs were also tested as a wearable impact force sensor to quantify soccer ball heading force, which was measured as  $291.3 \pm 51.0$  N for a vertical ball speed of  $7.8 \pm 1.5$  ms<sup>-1</sup> with an 8.2% average error compared to theoretical force values. It is believed the enhanced piezoelectric performance of these materials could provide a useful platform for wearable sensing and energy harvesting.

## 1. Introduction

In recent years, physiological data collection and analysis from wearable electronics have become a widespread part of daily life, with a particular focus on health and sports performance monitoring.<sup>[1–6]</sup> As a consequence, demand for accurate and stable wearable sensors for continuous physiological monitoring has been rapidly increasing. With advancement in nanofabrication techniques and flexible electronics, various routes for on-body real-time sensing have been realized, including monitoring for health conditions (such as diabetes mellitus,<sup>[1,4,7,8]</sup> cardiovascular diseases,<sup>[9–12]</sup> and COVID-19<sup>[13]</sup>), human motion detection,<sup>[14–16]</sup> and electrophysiology (e.g., electrocardiography [ECG]).<sup>[17–19]</sup>

An essential requirement for the advancement of continuous long-term wearable devices is for electronics to be self-powered and space-efficient, without the need for bulky unsustainable batteries. Methods of self-powering in research

literature have included using materials that can harvest energy from the human body and ambient environment<sup>[20]</sup> (e.g., from light,<sup>[21]</sup> heat,<sup>[22,23]</sup> or mechanical force<sup>[24,25]</sup>). In certain instances, energy harvesters can be used as active transducers for passive sensing by correlating the external stimuli (such as strain,<sup>[26–28]</sup> bending,<sup>[29]</sup> and impact force<sup>[30–34]</sup>) to the generated output.

The sensitivity and performance of these passive sensors is strongly dependent on the choice of sensor materials. Piezoelectric materials, such as piezoelectric ceramics and polymers, are capable of generating electrical energy from mechanical stimuli. While ceramics (such as lead zirconate titanate [PZT]) have shown very high efficiency in the interconversion of electrical and mechanical energy, they suffer from being toxic and brittle, which poses issues for wearable sensing applications.<sup>[35]</sup> Conversely, ferroelectric polymers (such as polyvinylidene fluoride [PVDF] and its copolymers) offer a mechanically flexible and nontoxic (lead-free) alternative to their ceramic counterparts.<sup>[36]</sup> PVDF has been used extensively in research and for commercial applications such as energy harvesting,<sup>[20,37]</sup> strain sensing,<sup>[26–28]</sup> audio transducers,<sup>[38]</sup> and western blotting.<sup>[39]</sup>

M. Chung, F. J. Diaz Sanchez, N. Radacsi

School of Engineering

The University of Edinburgh

King's Buildings, Mayfield Road, Edinburgh EH9 3JL, UK

E-mail: n.radacsi@ed.ac.uk

M. Chung, J. Schoeller, R. Stämpfli, R. M. Rossi

Empa, Swiss Federal Laboratories for Materials Science and Technology

Laboratory for Biomimetic Membranes and Textiles


Lerchenfeldstrasse 5, St. Gallen CH-9014, Switzerland

J. Schoeller

Department of Health Science and Technology

ETH Zürich

Zürich 8092, Switzerland

 The ORCID identification number(s) for the author(s) of this article can be found under <https://doi.org/10.1002/mame.202200520>

© 2022 The Authors. Macromolecular Materials and Engineering published by Wiley-VCH GmbH. This is an open access article under the terms of the Creative Commons Attribution License, which permits use, distribution and reproduction in any medium, provided the original work is properly cited.

DOI: 10.1002/mame.202200520

The crystalline domains of PVDF (namely,  $\alpha$ ,  $\beta$ ,  $\gamma$ , and  $\delta$ ) each offer different material characteristics, with the  $\beta$ -phase offering the highest piezoelectric response due to its well-oriented, non-centrosymmetric (polar) structure with an all *trans* planar zigzag conformation (TTTT).<sup>[40,41]</sup> Meanwhile, the  $\alpha$ -phase has a nonpolar structure with a *trans-gauche* twist conformation (TGTG') and is paraelectric.<sup>[40,41]</sup> Due to its lower potential energy, the  $\alpha$ -phase is more stable than the  $\beta$ -phase and therefore exists as the majority of the PVDF crystal structure.<sup>[40–43]</sup> To obtain a greater proportion of  $\beta$ -phase crystallinity, PVDF can be processed through a poling process in several different ways: for example through mechanical stretching,<sup>[44]</sup> annealing,<sup>[45]</sup> or by the application of an electric field.<sup>[46]</sup> In addition, copolymers such as trifluoroethylene (TrFE) can be combined with PVDF to enhance the crystallization of the  $\beta$ -phase during processing.<sup>[28,47]</sup>

Electrospinning is a simple and scalable fabrication technique capable of efficiently producing large quantities of polymer fibers on the nano- and microscale.<sup>[48,49]</sup> The conventional technique involves applying a sufficiently high voltage (in the range of kV) to a polymer solution droplet, which charges and stretches the liquid droplet (forming a characteristic droplet shape called a Taylor cone) due to the electrostatic repulsion overcoming the surface tension barrier.<sup>[50]</sup> At a critical point, where the Rayleigh limit is reached, a charged jet erupts from the Taylor cone surface and whips toward a grounded or biased collector. This time of flight assists in evaporating the polymer jet solvent, allowing the collection of dry uniform fibers.<sup>[50]</sup> The combination of the applied electric field and jet stretching during the electrospinning process provides a very useful method for obtaining a high percentage of  $\beta$ -phase PVDF crystallinity.<sup>[47,51,52]</sup> The PVDF fibrous structure also provides a mechanically flexible and chemically resistant platform with a high surface-to-volume ratio, ideal for surface modifications and functionalizations.<sup>[21]</sup>

Zinc oxide (ZnO) is an inherently piezoelectric material due to the non-centrosymmetric nature of its pristine wurtzite crystal structure with polar character along its (100) crystallographic direction.<sup>[53]</sup> It benefits from a wide bandgap (3.37 eV), low cost, ambient stability, biocompatibility, and simple crystal growth methods.<sup>[54]</sup> Electrospinning and ZnO nanomaterials have been used together extensively in research literature for a variety of applications such as energy harvesting,<sup>[29,32]</sup> photocatalytic sensing,<sup>[21,55,56]</sup> strain sensing,<sup>[26]</sup> field-effect transistors,<sup>[57]</sup> pressure sensing,<sup>[58]</sup> and biosensing.<sup>[59]</sup> Addition of ZnO nanomaterials into PVDF systems, and their subsequent hydrothermal growth to increase ZnO crystal size, have been shown to enhance piezoelectric performance and voltage output.<sup>[16,29–33,58,60–62]</sup> However, there has been difficulty in robustly attaching ZnO nanomaterials to the polymer surface, which can result in defects in the organic/inorganic contact, leading to trapped charges and poor sensor performance.<sup>[15,55]</sup> Recently, several studies have investigated the use of polydopamine (PDA) as an anchoring site for metal oxide nanomaterials and as an electron transfer layer to facilitate enhanced charge extraction in organic/inorganic systems.<sup>[15,55,63,64]</sup> It has been demonstrated that PDA can be used to coat numerous types of surfaces, regardless of material properties, using a simple oxidative self-polymerization technique in alkaline aqueous solutions.<sup>[65,66]</sup> Enhanced sensing performance has been shown utilizing PDA electron transfer layers for photocatalytic sensing with ZnO<sup>[55,56]</sup> and piezoelectric sensing with

barium titanate (BTO).<sup>[15,63]</sup> Despite this, the combination of electrospun PVDF-TrFE with PDA and hydrothermally grown ZnO has yet to be investigated for its piezoelectric output. It is hypothesized that exploiting the large surface area of the electrospun PVDF-TrFE will enable a large degree of ZnO coating, providing an enhanced piezoelectric response.

In this work, ZnO nanoparticles (NPs) were attached to PVDF-TrFE electrospun fibers (EFs), assisted by a self-polymerized surface coating of PDA. The PVDF-TrFE EFs were prepared using a high-throughput nozzle-free electrospinning process for efficient scalability. ZnO NPs were then grown into nanowires (NWs) through a process of hydrothermal growth before piezoelectric performance of PVDF-TrFE, ZnONPs@PVDF-TrFE, and ZnONWs@PVDF-TrFE EFs were compared using different low-cost, home-built impact force testing methods. The materials were investigated for their potential use as a passive wearable impact force sensing platform by calibrating with impact forces up to 970 N and incorporating them into a wearable headband for measuring the impact of a soccer ball with the head. It is believed that these materials could offer a viable platform for wearable impact force sensing during sports activities as well as other piezoelectric sensing and energy harvesting mechanisms.

## 2. Experimental Section

### 2.1. Materials

Solvane® 300/P300 PVDF-TrFE (70:30 ratio), polyethylene oxide (PEO) ( $M_w = 100\,000$ ),  $\geq 99\%$  lithium chloride salt (LiCl),  $> 97\%$  zinc oxide (ZnO) nanopowder with  $< 50$  nm particle size, 99.8% *N,N*-dimethylformamide (DMF), 98% zinc nitrate hexahydrate,  $\geq 99\%$  hexamethylenetetramine (HMTA),  $> 98\%$  dopamine hydrochloride, and  $> 99\%$  Tris hydrochloride were purchased from Sigma-Aldrich and used without further purification. Sylgard 184 polydimethylsiloxane (PDMS) with curing agent was also purchased from Farnell UK.

### 2.2. Fabrication of Electrospun Piezoelectric Impact Sensors

**Figure 1** outlines the fabrication process for the electrospun piezoelectric impact sensors. Electrospun PVDF-TrFE fibrous mats were fabricated using a high-throughput, nozzle-free electrospinning method established previously by Diaz Sanchez et al.<sup>[67]</sup> Briefly, PVDF-TrFE and PEO at a 50:3 ratio (w/w) were dissolved in a solvent system of DMF and DI water (50:3 w/w) for 24 h at 80 °C (200 RPM magnetic stirring) to obtain an overall concentration of 12 wt%. 0.75 wt% LiCl salt was then added relative to the polymer solution weight and left to stir for a further 24 h. The solution was then reduced in temperature to 40 °C before being transferred to a home-built nozzle-free electrospinning setup (Figure 1a). Details of the nozzle-free electrospinning setup can be found in a technical paper from our group.<sup>[68]</sup> Here, the solution was used to coat a rotating positive electrode (5 RPM) in a Teflon bath, which was biased with +30 kV. A rotating collector, wrapped in aluminum foil, was negatively biased with –30 kV and was set to turn at 30 RPM. The distance between electrodes was 15 cm and the enclosed chamber was maintained at a temperature of 33 °C and a relative humidity ranging between 5% and 7%, by use of a heat gun.

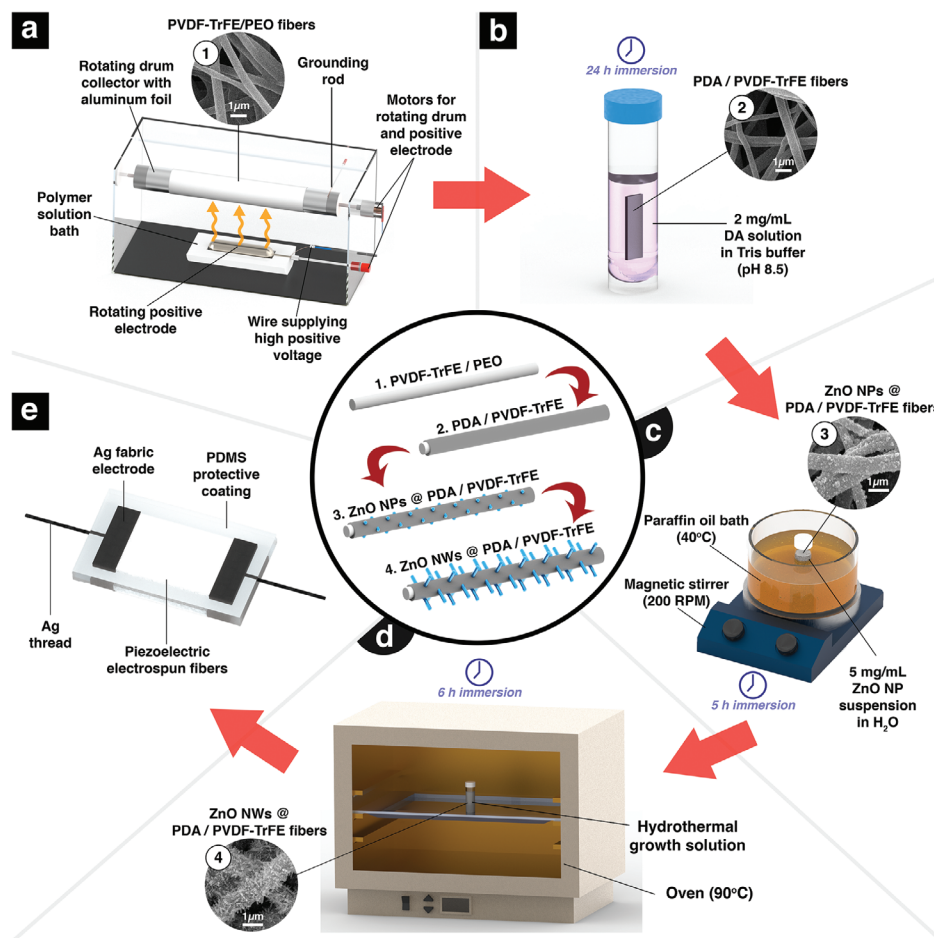


**Figure 1.** Fabrication process of ZnO/PVDF-TrFE electrospun impact force sensors with a) electrospinning of PVDF-TrFE/PEO EFs using a nozzle-free setup; b) immersion of PVDF-TrFE EFs in a 2 mg mL<sup>-1</sup> DA solution in Tris buffer (pH 8.5) for 24 h; c) immersion of PDA/PVDF-TrFE EFs in a 5 mg mL<sup>-1</sup> ZnO NP suspension in DI H<sub>2</sub>O at 40 °C for 5 h with gentle stirring at 200 RPM; d) hydrothermal treatment for 6 h at 90 °C of ZnONPs@PDA/PVDF-TrFE EFs for crystal growth into ZnO NWs; and e) assembly of piezoelectric electrospun impact sensors by attachment of Ag fabric electrodes and encasement in PDMS.

The EFs were then removed from the rotating drum and cut into samples of 15 × 20 mm. PVDF-TrFE/PEO EFs were then immersed in deionized (DI) water for 24 h at 80 °C to remove non-piezoelectric PEO from the electrospun mats. To obtain ZnO-nanomaterial-modified PVDF-TrFE EFs, a method proposed by Kim et al.<sup>[56]</sup> was utilized where electrospun samples were immersed in a dopamine hydrochloride solution (2 mg mL<sup>-1</sup> of dopamine hydrochloride in 10 × 10<sup>-3</sup> M Tris buffer at pH 8.5) for 24 h at 23 °C to self-polymerize PDA on the surface of the fibers. Next, PDA/PVDF-TrFE EFs were immersed in a ZnO nanopowder suspension (5 mg mL<sup>-1</sup> ZnO nanopowder in DI water) and were shaken at 200 rpm for 5 h at 40 °C to facilitate attachment of ZnO NPs to the free catechol groups of the PDA surface layer. Samples were then washed twice with DI water in an ultrasonic bath for 10 min each washing cycle before being washed again in EtOH. The ZnONPs@PVDF-TrFE EFs were then dried at 40 °C overnight.

To obtain ZnONWs@PVDF-TrFE, ZnONPs@PVDF-TrFE EF samples were immersed in an aqueous solution containing 25 × 10<sup>-3</sup> M zinc nitrate hexahydrate and 100 × 10<sup>-3</sup> M hexam-

ethylenetetramine (HMTA) for up to 6 h at 90 °C. This is a well-established low cost, low temperature hydrothermal growth process.<sup>[69–74]</sup> Samples were then washed and dried using the same method as with the ZnONPs@PVDF-TrFE EFs above.

Finally, to obtain the piezoelectric impact sensors, PVDF-TrFE, ZnONPs@PVDF-TrFE, and ZnONWs@PVDF-TrFE samples had Ag fabric electrodes attached to either side through stitching of conductive Ag thread. Subsequently, the electrospun impact sensors were coated in transparent Sylgard 184 elastomer PDMS (mixed in a 10:1 weight ratio of Sylgard 184 to the curing agent) and cured at 90 °C for 1 h to provide insulation and protection for the samples. The impact sensors were then stored at room temperature for a further 24 h to ensure all PDMS had been completely cured.

### 2.3. Characterization of Electrospun Piezoelectric Impact Sensors

Morphologies of electrospun NFs were visually inspected using a JSM-IT100 scanning electron microscope (SEM) (JEOL Ltd.,

Japan). Fiber and nanomaterial dimensions were calculated using ImageJ software by taking 50 measurements per X2000 magnification SEM image.

X-ray photoelectron spectroscopy (XPS) spectrograms were recorded on a Quantum 2000 X-ray photoelectron spectrometer (Physical Electronics, USA) equipped with an Al K $\alpha$  monochromatic source (1486.6 eV). All the spectra were recorded in fixed analyzer transmission mode using a nominal X-ray beam spot size of 200  $\mu$ m. The atomic fractions ( $\varphi_a$ ) of detectable elements were measured from the survey spectra (pass energy of 117.40 eV with an energy step of 0.5 eV) using the peak intensities ( $I_a$  = peak intensity of atom of interest,  $I_i$  = each individual atom peak intensity) Equation (1)

$$\varphi_a = \frac{\frac{I_a}{RSF_a}}{\sum_i^n \frac{I_i}{RSF_i}} \quad (1)$$

where the relative sensitivity factors (RSF) were obtained from the analysis software of the spectrophotometer (Multipak<sup>®</sup>) and Shirley backgrounds were subtracted to allow for the estimation of the peak intensity ( $I_i$ ). For high-resolution region scan, a pass energy of 93.80 eV with an energy step of 0.80 eV was used. The data were processed with CasaXPS (Casa Software Ltd., Teignmouth, UK) where carbon 1s was used for calibration of the spectra at 284.5 eV.

Attenuated total reflectance Fourier transform infrared (ATR-FTIR) spectra were collected on a Varian 640-IR spectrometer (Agilent Technologies, USA). For each sample, spectra were recorded from 600 to 4000  $\text{cm}^{-1}$  with a resolution of 1  $\text{cm}^{-1}$ .

X-ray diffraction (XRD) analysis was conducted using a D2 Phaser (Bruker, USA) with a 300 W Cu K $\alpha$  X-ray source (wavelength = 1.5406 Å).

## 2.4. Impact Testing of Electrospun Piezoelectric Impact Sensors

The responses of the piezoelectric samples to applied impact forces were measured using two different homebuilt setups. The first setup (Figure 5d) included a 3D-printed horizontal poking device which was designed using Solid Edge 2020 (Siemens PLM Software, USA) and 3D-printed using an Ultimaker 3 (Ultimaker, Netherlands) with a polylactic acid filament. The stepper motor was controlled using an Arduino Mega 2560 Rev3 microcontroller and applied consistent impact forces to samples at a rate of 3.6 Hz. To measure the impact force, a Model FSR 402 circular force-sensing resistor (Interlink Electronics, USA), with 12.7 mm diameter and sensitive range of 0.1–10.0 N, was attached to the impact tool. As per guidelines suggested in the manufacturer datasheet, the force-sensing resistor was connected in a voltage divider configuration and was supplied with  $\pm 9$  V from a battery. A resistor ladder circuit with two different resistive loads (1.6 and 15.1 M $\Omega$ ) and an Agilent MSO6054A mixed signal oscilloscope (Agilent Technologies, USA) were used to measure the electrospun piezoelectric sample output voltage. All data were extracted as binary (BIN) files and analyzed using a bespoke MATLAB (MathWorks, USA) code. Each sample was poked a total of 360 times, however, filtering using a MATLAB code was utilized to remove any impacts where the commercially bought force sensor did not record a measurement correctly (<80% of the mean

peak value recorded with the force-sensing resistor) (Figure S1a, Supporting Information).

The second setup (Figure 6c) involved testing the piezoelectric response of the samples with increasing impact forces using a guided free fall mechanism. To achieve this, a 2 m long polycarbonate tube (40 mm outer diameter and 36 mm inner diameter) was held vertically using a leveled wooden structure and a hollow 3D-printed cylindrical container was dropped onto the samples from the top of the tube with the sample secured at the bottom. To increase the weight of the 3D-printed tube (initial mass = 44 g), 12 g cylindrical lead weights were inserted and held in place using a PDMS stopper. A PDMS shock absorber (28 mm diameter, 15 mm thickness) was casted onto the bottom of the 3D-printed tube to prevent the plastic structure from fracturing at higher weights. Masses between 25 and 570 g were dropped three times for each mass onto each sample with the entire experiment repeated twice. The voltage output was recorded for each dropped mass using an Agilent MSO6054A mixed signal oscilloscope (Agilent Technologies, USA) with a resistive load of 1 M $\Omega$ . To find the impact force, theoretical and experimental procedures were used following methods outlined by PCB Piezotronics for impact force testing using piezoelectric force sensors.<sup>[75]</sup> In both cases, impact force was calculated using Equation (2)

$$F_{\text{impact}} = ma = m \left( \frac{v_{\text{int}} - v_{\text{fin}}}{t_{\text{contact}}} \right) \quad (2)$$

Here,  $a$ ,  $m$ ,  $v_{\text{int}}$ ,  $v_{\text{fin}}$ , and  $t_{\text{contact}}$  are the acceleration, mass, initial velocity (immediately before impact), final velocity (immediately after impact), and time of contact, respectively. For the theoretical impact force value, the law of conservation of energy assumes the kinetic energy after an event is equal to the potential energy before an event. Therefore, assuming negligible drag forces due to air resistance, the velocity of the falling mass can be calculated using Equation (3)

$$v_{\text{int}} = \sqrt{2gh} \quad (3)$$

In this case,  $g$  is the acceleration of gravity and  $h$  is the height the mass was dropped from. Therefore, if it is assumed that there is a perfect rebound between the falling mass and the sample, velocity will be conserved but in opposite directions giving Equation (4) below for the theoretical impact force

$$F_{\text{theory}} = m \left( \frac{2\sqrt{2gh}}{t_{\text{contact}}} \right) \quad (4)$$

However, in reality the rebound of the mass will not be perfect and so the experimental velocity values were found by recording each impact with a high-speed camera (240 fps, iPhone XR camera) to utilize the distance the mass travelled in one frame (0.004 s) immediately before and after impact using ImageJ software. This could be used to obtain the real velocity values, which could then be inserted into Equation (2) to calculate the experimental impact force values ( $F_{\text{exp}}$ ).

To find  $t_{\text{contact}}$ , a method using the pulse width of the impact peaks was utilized to approximate the time of contact between the mass and the sample.<sup>[75]</sup> This pulse width was taken as the full



duration at half maximum (FDHM) of the absolute peak-to-peak voltage output (Figure S1c, Supporting Information).

To characterize the soccer ball impact force, a drop test system<sup>[76]</sup> was used (Figure 7c). The flat anvil of Ø 130 mm was equipped with a piezoelectric load cell (Kistler Group, Winterthur, Switzerland, type 9361B, ±60 kN) whose signal was processed with a charge meter (Kistler Group, Winterthur, Switzerland, type 5015A). The sensors were each positioned in the center of the anvil and connected to the oscilloscope (Rigol Technologies EU GmbH, Gilching, Germany, model MSO1104Z, sample rate 50 kHz) via a 10:1 probe (input resistance 10 MΩ). The second channel of the oscilloscope was connected to the ±10 V output of the charge meter for synchronous recording of the two signals. A FIFA Quality Pro soccer ball (Umbro, Neo Precision, weighing value: 423.3 g, radius 109.6 ± 0.3 mm, pressure 0.80 bar) was dropped three times from five different heights (1.00, 1.50, 2.00, 3.00, 4.00 m) on each of the three sensors.

Demonstrations of all three impact sensor calibration techniques can be viewed in Video S1 (Supporting Information).

Welch's *t*-tests were used to compare the means of the piezoelectric EF samples responses to the horizontal impact force testing. The mean values (V/N) of each dataset were considered statistically significantly different if  $p < 0.05$ .

## 2.5. Sensing of Soccer Ball Head Impact Forces

One male subject ( $n = 1$ ,  $h = 182$  cm,  $w = 78$  kg) was utilized for soccer ball heading force tests. A ZnONWs@PVDF-TrFE EF piezoelectric impact sensor was integrated into an elastic headband and worn on the head of the participant (Figure 7b). Informed written consent from all participants or next of kin was obtained prior to this research. The sensor was connected to an Agilent MSO6054A mixed signal oscilloscope (Agilent Technologies, USA). A regulation soccer ball (size 5, 0.81 bar, 426 g) was dropped from 2 m above the subject vertically downwards onto the stationary subject's forehead to simulate a standard header experienced in a soccer match. This was repeated three times. A high-speed camera (240 fps, iPhone XR camera) was used to capture the video footage and calculate  $F_{\text{exp}}$  using Equation (2) (details shown in Section S6, Supporting Information).

## 3. Results and Discussion

### 3.1. Electrospun Piezoelectric Impact Force Sensor Fabrication

The process for producing the electrospun piezoelectric impact force sensors is outlined in Figure 1. Firstly, electrospinning of PVDF-TrFE/PEO fibers was achieved using a nozzle-free setup (Figure 1a) with a throughput of 11.2 g h<sup>-1</sup> of EFs collected on the rotating drum. These EFs were inspected for their morphology using SEM, with the images shown in Figure 1 and Figure S2 (Supporting Information). The average fiber diameter was found as 764 ± 207 nm, which is consistent with results found in previous work.<sup>[67]</sup> Demonstrated in our previous work,<sup>[67]</sup> PEO was added to enhance electrospinnability of the polymer solution and to increase the surface area of the fibrous membranes, while LiCl salt was added to increase the  $\beta$ -phase content of the PVDF-TrFE EFs by raising the conductivity of the solution.<sup>[77,78]</sup>

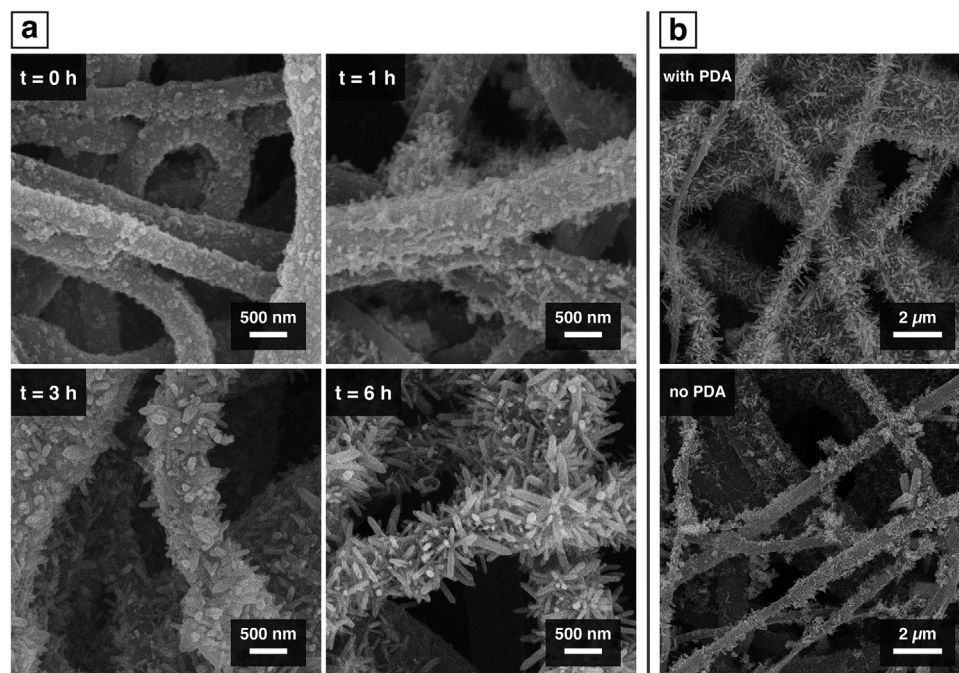
After electrospinning, PVDF-TrFE/PEO EFs were soaked in DI H<sub>2</sub>O at 80 °C for 24 h to dissolve as much of the low concentration of PEO as possible present in the fibers. With this processing step, the fibers are herein labeled "PVDF-TrFE EFs" for simplicity as PEO concentration in the electrospun membranes is assumed to be negligible.

Figure 1b,c outlines the process for ZnO NP attachment to the PVDF-TrFE EFs. The fibers were immersed in an aqueous solution of dopamine hydrochloride in slightly alkaline conditions (in Tris buffer, pH 8.5) to enable self-polymerization of dopamine into PDA, which provides a simple method of spontaneous coating on the fiber surface via catechol/amine group bonding.<sup>[55]</sup> In this mechanism, some PDA chain catechol groups remain unbonded to the fiber surface, which have been hypothesized to subsequently provide additional sites to anchor metal oxide nanoparticles.<sup>[56]</sup> ZnO NP attachment to the PDA/PVDF-TrFE EFs was facilitated in a 5 mg mL<sup>-1</sup> suspension of ZnO powder in DI water at 40 °C with gentle stirring at 200 RPM for 5 h before being visually inspected with SEM (Figure 2a,  $t = 0$  h).

Figure 1d displays the method for scalable, low-cost, low-temperature solution growth of ZnO NPs into NWs using hydrothermal treatment. An aqueous solution of 25 × 10<sup>-3</sup> M zinc nitrate and 100 × 10<sup>-3</sup> M HMTA was used for hydrothermal growth by immersing the ZnONPs@PVDF-TrFE EFs at 90 °C for 6 h. The low-temperature nature of this process enables flexible polymer substrates with low melting points, such as the PVDF-TrFE EFs, to be used as a basis for ZnO growth without detrimental effects. Dissolution of zinc nitrate at elevated temperatures and thermal degradation of HMTA release Zn<sup>2+</sup> and hydroxide ions, respectively, which react to grow ZnO on the attached ZnO NPs present on the PDA/PVDF-TrFE EFs.<sup>[72,73]</sup> SEM images were taken of ZnONWs@PVDF-TrFE with different growth times (Figure 2a).

As the time of growth increases up to 6 h, the length of the attached ZnO crystals also increase (average length = 365 ± 58 nm, average diameter = 91 ± 21 nm after 6 h growth), originating from the (001) polar Zn<sup>2+</sup> face and growing along the  $+c$ -axis.<sup>[74]</sup> As the process of Ostwald ripening energetically favors larger crystals, the nucleation sites provided by the attached ZnO NPs will be favored for further growth as opposed to any spontaneous formation of tiny crystallites in solution. In similar studies, homogenous crystal growth appears to reach a limit after 6 h, which has been suggested is due to consumption of all free Zn<sup>2+</sup> available in solution.<sup>[79]</sup> ZnONWs@PVDF-TrFE EFs were inspected after immersion in hydrothermal growth solution for 12 h (Figure S3, Supporting Information), where it was observed that homogenous coverage of ZnO NWs was lost and instead a smaller number of larger ZnO crystals were found in the EF membrane (average length = 1089 ± 423 nm, average diameter = 261 ± 98 nm). This supports the hypothesis that free Zn<sup>2+</sup> in solution is no longer available to react and so Ostwald ripening occurs by dissolving the smaller attached ZnO NWs to contribute to the growth of the larger crystals, resulting in far fewer ZnO NWs.

To examine the effect of the PDA layer on the attachment of ZnO nanomaterials to the EFs, ZnONWs@PVDF-TrFE EFs with and without PDA were inspected using SEM after 40 min total of ultrasonication. From Figure 2b, it can be observed that PVDF-TrFE EFs with a PDA layer facilitate homogenous attachment of



**Figure 2.** SEM images after hydrothermal treatment on ZnONPs@PVDF-TrFE EFs with a) ZnO crystal growth after 0, 1, 3, and 6 h on PDA/PVDF-TrFE EFs; and b) ZnO crystal growth on PVDF-TrFE EFs with and without a PDA self-polymerization step (after a total of 40 min of ultrasonication).

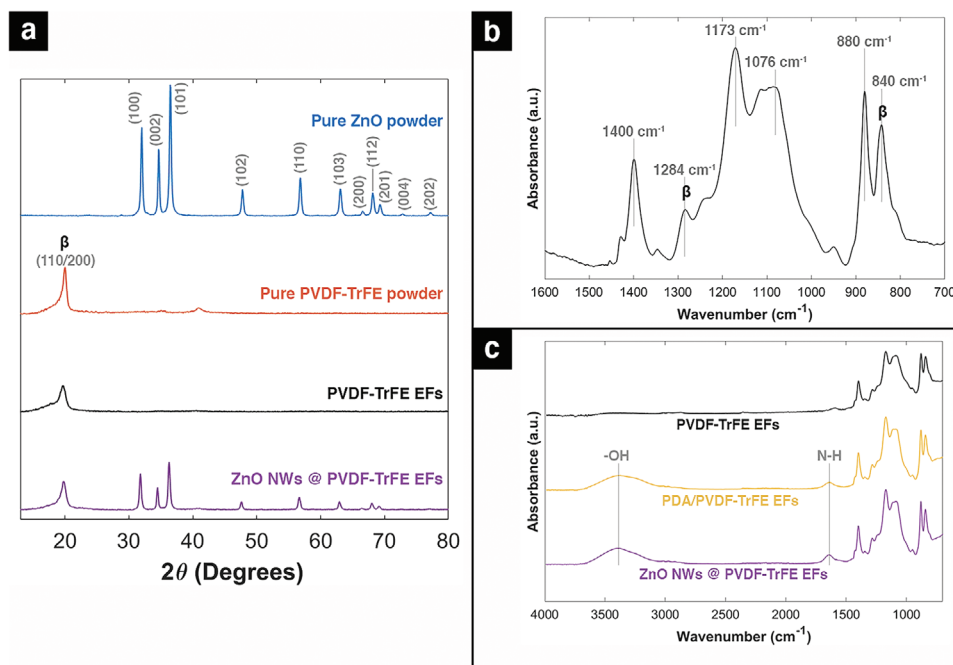
ZnO NPs with good fiber coverage while the EFs without PDA suffer from sparse coverage due to poor attachment. This is in agreement with published literature where a PDA layer was used to attach ZnO NPs to EFs.<sup>[56]</sup>

Figure 1e shows an illustration of the final electrospun piezoelectric impact sensor, which was produced by stitching fabric Ag electrodes to either side of EF membranes with Ag thread. This ensured a high surface area of attachment to provide a good electrical contact for measuring piezoelectric outputs. To protect the impact sensors from physical damage, contamination, electrical interference, and ambient effects, the piezoelectric EFs with attached Ag electrodes were encased in the transparent PDMS Sylgard 184. This protection is particularly important for ZnO nanomaterials, which are affected by humidity and can readily adsorb contaminants from the ambient environment.<sup>[71]</sup>

The primary reason for the use of electrospinning as a processing technique for PVDF-TrFE was to ensure that the high electric field and mechanical polymer jet stretching experienced during fabrication would result in  $\beta$ -phase crystallinity in the PVDF-TrFE EF membranes. This was investigated and confirmed using XRD and ATR-FTIR techniques shown in Figure 3a–c, respectively. From the XRD analysis, the peaks of the PVDF-TrFE EFs and ZnONWs@PVDF-TrFE EFs spectra were compared to the spectra of the pure powders. An intense peak was observed at  $2\theta = 20.0^\circ$  for both PVDF-TrFE powder and EFs, which corresponds to the (110)/(200) reflection of orthorhombic  $\beta$ -phase PVDF crystallinity. In pure PVDF, an intensive peak at  $2\theta = 18.4^\circ$  and a medium peak at  $2\theta = 26.6^\circ$  should be expected, which would be attributed to (020) and (021) monoclinic  $\alpha$ -phase crystal reflections, respectively.<sup>[80]</sup> However, these are absent in the XRD spectra in Figure 3a, confirming that PVDF-TrFE crystallizes predominantly in the  $\beta$ -phase.

The XRD peaks of the pure ZnO powder correspond to the different crystal planes of a ZnO wurtzite crystal structure<sup>[81]</sup> (JCPDS card no. 01-079-2205). It can be observed that the same distinct peaks are present in the spectrum of ZnONWs@PVDF-TrFE EFs, confirming the presence of piezoelectric ZnO wurtzite nanomaterials on the surface of the EFs. As the (110)/(200)  $\beta$ -phase peak position does not shift after ZnO attachment to the PVDF-TrFE EFs and subsequent hydrothermal treatment step, it can be concluded that the hydrothermal solution growth method is undertaken at a low enough temperature to not affect the PVDF-TrFE crystal structure.<sup>[21]</sup>

The ATR-FTIR spectrum of PVDF-TrFE EFs is shown in Figure 3b between wavenumbers of 700 and 1600  $\text{cm}^{-1}$ . Cai et al.<sup>[80]</sup> previously collected ATR-FTIR analytical data of PVDF from >100 sources where it was found that many of the peaks have been disputed as to their corresponding crystal phases ( $\alpha$ ,  $\beta$ ,  $\gamma$ , or combinations of phases). The peaks with the largest majority of agreement among sources that correspond to only  $\beta$ -phase crystallinity were found to be at 840  $\text{cm}^{-1}$  ( $\text{CF}_2$  symmetrical stretch) and  $\approx 1280 \text{ cm}^{-1}$  ( $\text{CH}_2$  scissoring and  $\text{CF}_2$  symmetrical stretch).<sup>[29,47,82]</sup> From similar studies,<sup>[47,80,83]</sup> it is known that the clear peaks corresponding to PVDF  $\alpha$ -phase crystallinity are at 765, 795, and 975  $\text{cm}^{-1}$ . These are not visible in the PVDF-TrFE EF spectrum shown in Figure 3b, reinforcing the XRD results concerning the dominant presence of  $\beta$ -phase crystallinity. Meanwhile, Figure 3c shows the wider range ATR-FTIR spectra of PVDF-TrFE EFs, PDA/PVDF-TrFE EFs, and ZnONWs@PVDF-TrFE EFs. The spectra all share the same peaks except for a broad peak at 3380  $\text{cm}^{-1}$  and another peak at 1643  $\text{cm}^{-1}$ , which both appear after the PDA self-polymerization step. These peaks can be attributed primarily to the presence of  $-\text{OH}$  bonding (3380  $\text{cm}^{-1}$ ) from catechol groups and the  $\text{N}-\text{H}$  bonding (1643  $\text{cm}^{-1}$ )



**Figure 3.** XRD and ATR-FTIR spectral data for PVDF-TrFE and ZnO materials. a) XRD spectra comparison of pure ZnO nanopowder, pure PVDF-TrFE powder (70:30), PVDF-TrFE EFs, and ZnONWs@PVDF-TrFE EFs; b) ATR-FTIR spectrum of PVDF-TrFE EFs highlighting  $\beta$ -phase crystallinity peaks; c) ATR-FTIR spectra comparison of PVDF-TrFE EFs, PDA/PVDF-TrFE EFs, and ZnONWs@PVDF-TrFE EFs.

from the primary amine of the PDA coated layer. A contribution to the broad hydroxyl peak may also be due to the presence of Zn-OH after the addition of ZnO nanomaterials.

XPS analysis (Figure 4) was conducted on PVDF-TrFE, PDA/PVDF-TrFE, and ZnONWs@PVDF-TrFE EFs to investigate the elemental and molecular surface composition after each fabrication step. Table 1 summarizes the atomic concentrations of each sample from the XPS survey scans.

As can be seen from the XPS survey scans in Figure 4a and atomic concentration data in Table 1, for each sample, C, F, and O are present on the surface of the EFs. The concentrations of polymers in the electrospinning solution were used alongside empirical formulae to estimate atomic percentages. For PVDF-TrFE/PEO EFs (before the soaking step in DI water), the concentration of F is lower than anticipated ( $\approx 51\%$  expected) while C and O are higher than projected ( $\approx 48\%$  and  $\approx 1\%$  expected, respectively). It is unlikely that PEO tends towards the surface of the fibers during electrospinning, as fluorinated polymers have been shown to orient towards the surface with phase separation of polymer blends during electrospinning due to their lower surface energy.<sup>[84,85]</sup> Therefore, the higher than expected C and O could instead be attributed to surface imperfections or adsorption of moisture onto the fiber surface. Nevertheless, a decrease in C and O concentration and an increase in F concentration are observed after the PVDF-TrFE/PEO EFs were soaked in DI water for 24 h at 80 °C. As these samples were dried and stored in the same conditions as the unsoaked samples, it can be assumed the reduction in C and O concentration on the surface of the EFs is due to the removal of PEO from the EF membranes, however, it cannot be proven that all PEO is removed during the soaking step.

From previous studies on XPS analysis of PVDF-TrFE, three main peaks are present within the C 1s region scan at binding energies of around 292, 290, and 288 eV that correspond to the  $\text{CF}_2$ , CFH, and  $\text{CH}_2$  bonds, respectively.<sup>[86–89]</sup> These were fitted into the C 1s region scans of PVDF-TrFE EFs and PDA/PVDF-TrFE EFs using CasaXPS software and can be seen in Figure 4b. The same peaks were fitted into the C 1s region scan of unsoaked PVDF-TrFE/PEO EFs, which can be seen in Figure S5 (Supporting Information). From theoretical atomic ratios calculated from empirical formulae, it should be expected from a 70:30 ratio of PVDF to TrFE that the  $\text{CF}_2$  peak area should be approximately three times greater than the CFH peak area, while the  $\text{CH}_2$  peak area should be around two times greater than the CFH peak area. In the case of the analyzed samples in Figure 4b, it was the  $\text{CH}_2$  peak that had the largest area. This may be due to adsorbed hydrocarbon contaminants in the form of C=O bonds, which share a similar binding energy as the CFH and  $\text{CH}_2$  peaks,<sup>[87]</sup> or it could be due to prolonged X-ray irradiation during XPS measurement which has been shown to cause defluorination of fluorinated polymer samples over time.<sup>[89]</sup> In the C 1s region scan of PVDF TrFE EFs, the peak fitting revealed two peaks at 286 and 284 eV corresponding to C–O bonds and C–H bonds, respectively.<sup>[87,88]</sup> Again, the C–O peak can be attributed to adsorbed moisture/contaminants or small concentrations of residual PEO.

After the PDA self-polymerization step, a N 1s peak appears with a  $3.0 \pm 0.3\%$  atomic concentration (Figure 4a) as well as an observed increase in C and O atomic concentrations. As N can only be found in the amine group of the polymeric backbone of PDA, we can assume that the PDA coating step was successful. This is further confirmed by the increase in C and O related

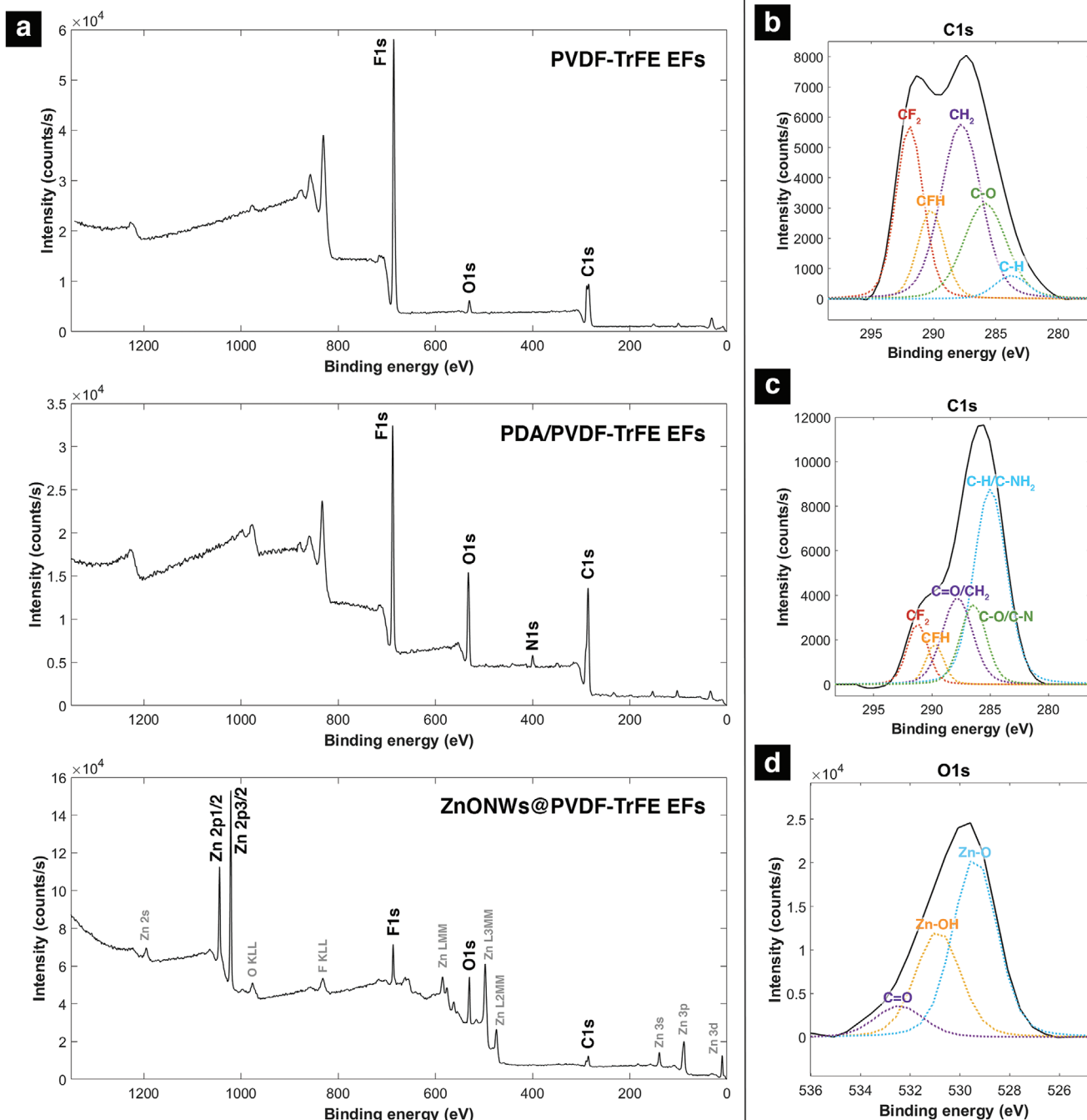


**Figure 4.** XPS data of piezoelectric EF materials with: a) XPS survey scans of PVDF-TrFE EFs (top), PDA/PVDF-TrFE EFs (middle), and ZnONWs@PVDF-TrFE EFs (bottom); b) region scan of C1s of PVDF-TrFE EFs; c) region scan of C1s of PDA/PVDF-TrFE EFs; and d) region scan of O1s of ZnONWs@PVDF-TrFE EFs.

to the benzene ring and hydroxyl bonds of the catechol groups in PDA. As there is still a relatively high atomic concentration of F in the PDA/PVDF-TrFE EF sample, the PDA layer is either thin enough for PVDF-TrFE to be detected or the PDA layer is inhomogeneous. However, the standard deviations of the measured atomic concentrations are low, which implies the concentrations are consistent over several areas of the PDA/PVDF-TrFE EF membrane. Therefore, it is more likely the PDA layer is very

thin as indicated by the fact that only the electrons near the surface (<10 nm deep) can be emitted without losing energy in XPS analysis.<sup>[90]</sup> The C 1s region scan of PDA/PVDF-TrFE (Figure 4b) displayed an increase in the C=O/CH<sub>2</sub> as well as a large increase in the peak at 284 eV, which was identified as C-H/C-NH<sub>2</sub>. The peak at 286 eV also saw an increase due to contributions from C-O and C-N bonds. These results are consistent with XPS analysis of PDA coatings from literature<sup>[91–93]</sup> and confirm



**Table 1.** XPS atomic concentration data for piezoelectric EF samples.

Electrospun sample	Atomic concentration [%]					
	C 1s	F 1s	O 1s	N 1s	Zn 2p1/2	Zn 2p3/2
PVDF-TrFE/PEO	59.3 ± 0.5	36.0 ± 0.3	4.7 ± 0.3	–	–	–
PVDF-TrFE (after soak)	53.6 ± 0.4	43.2 ± 0.6	3.3 ± 0.2	–	–	–
PDA/PVDF-TrFE	60.6 ± 0.5	21.7 ± 0.2	14.8 ± 0.2	3.0 ± 0.3	–	–
ZnONPs@PVDF-TrFE	33.2 ± 1.8	19.7 ± 2.1	24.6 ± 1.0	–	12.1 ± 1.1	10.4 ± 1.0
ZnONWs@PVDF-TrFE	27.6 ± 0.9	14.6 ± 0.8	27.8 ± 0.3	–	14.6 ± 0.0	15.4 ± 0.5

Note: Additional XPS survey and region scan data can be found in Figure S4 (Supporting Information).

the presence of catechol groups utilized for ZnO nanomaterial anchoring.

For ZnONWs@PVDF-TrFE EFs, several peaks associated with Zn appeared in the corresponding XPS survey scan in Figure 4a. The core level XPS region that is most commonly used to quantify ZnO is Zn 2p, which appears as a doublet with spin–orbit splitting. The two Zn 2p spin–orbit peaks are observed in the ZnONWs@PVDF-TrFE EFs XPS survey scan with Zn 2p3/2 at  $1021.0 \pm 0.1$  eV and Zn 2p1/2 at  $1044.0 \pm 0.4$  eV (Figure S6, Supporting Information). Meanwhile, for ZnONPs@PVDF-TrFE, the Zn 2p3/2 peak is located at  $1020.7 \pm 0.3$  eV, with the Zn 2p1/2 peak at  $1043.4 \pm 0.2$  eV (Figure S6, Supporting Information). The binding energy difference between the two spin–orbit peaks remains constant (23 eV) for both ZnO NPs and ZnO NWs, while an overall binding energy shift of  $\approx +0.6$  eV when the ZnONPs are hydrothermally grown into ZnO NWs can be observed. This is consistent with other XPS results from literature.<sup>[69,81,94]</sup> The overall atomic concentrations of O 1s and Zn 2p also increase with hydrothermal treatment, confirming the growth of the ZnO crystals. The peak fitting of the O 1s region scan of ZnONWs@PVDF-TrFE EFs (Figure 4b) identifies three peaks: a Zn–O peak at 529.6 eV, a Zn–OH peak at 531.0 eV, and a C=O peak at 532.6 eV. These results align well with other hydrothermally grown ZnO NW XPS data in literature.<sup>[81,95]</sup>

Overall, from visual inspection using SEM, and from the surface and crystal analysis at the various stages of the electrospun piezoelectric impact sensor fabrication process, it can be concluded that PVDF-TrFE EFs were produced with a high level of  $\beta$ -phase crystallinity, while subsequent PDA coating and ZnO nanomaterial attachment steps were successful and provided good coverage and robust anchoring to the electrospun membrane.

### 3.2. Impact Force Sensor Testing and Calibration

Electrospun PVDF-TrFE piezoelectric impact sensors, with and without added ZnO nanomaterials, were compared for their voltage output using two different methods. The first method involved applying a consistent horizontal impact force at regular time intervals by using a homemade, low-cost 3D-printed poking device displayed in Figure 5d. A stepper motor was used to drive the linear actuator with a force application frequency of 3.6 Hz. A commercially available force sensor was attached to the front of

the poking part to measure the applied impact force to the electrospun piezoelectric sample with every actuation. The piezoelectric sample was connected to a resistor ladder circuit to check the output voltage signal at different resistive loads and was analyzed using an oscilloscope.

An example output signal can be seen in Figure 5a,c where a ZnONWs@PVDF-TrFE sample was impacted 180 times in 50 s. In this example, the static charge produced with each impact is measured as a momentary voltage across the resistive load, which provides a leakage pathway for the charge. When the applied force is released, electrons are drawn back through the resistor to neutralize the piezoelectric sample, generating a momentary negative voltage. With this effect, the output signal resembles an AC response, with the peak-to-peak voltage ( $V_{pp}$ ) proportional to the impact force and the positive and negative voltage peaks denoting the force application and release cycles, respectively. This process was repeated for different electrospun piezoelectric samples at two different loads (1.6 and 15.1 M $\Omega$ ) and the average output  $V_{pp}$  per Newton of applied impact force (V/N) was calculated in each case. Figure 5b compares the output V/N of two PVDF-TrFE, two ZnONPs@PVDF-TrFE, and four ZnONWs@PVDF-TrFE EF piezoelectric samples with a load of 15.1 M $\Omega$ . For a comparison of the eight samples at a load of 1.6 M $\Omega$ , see Section S7 (Supporting Information).

The average impact force applied across all eight samples with the two different loads was  $2.6 \pm 1.0$  N (total sample number = 4933). With a measured impact contact area of 2.6 cm<sup>2</sup>, the average impact pressure was calculated as  $10.0 \pm 3.8$  kPa. The V/N of the PVDF-TrFE samples were  $9.1 \pm 2.0$  and  $10.4 \pm 1.7$  V N<sup>−1</sup>, while addition of the PDA coating and ZnO NPs gave a V/N of  $13.1 \pm 2.8$  and  $10.0 \pm 4.4$  V N<sup>−1</sup>. Meanwhile, the four V/Ns of the ZnONWs@PVDF-TrFE EF samples were  $28.5 \pm 3.7$ ,  $21.3 \pm 2.6$ ,  $25.8 \pm 3.5$ , and  $24.5 \pm 3.2$  V N<sup>−1</sup>. Table 2 also displays the comparison between the overall means and standard deviations of each sample type. From these results it can be seen that the addition of PDA and ZnO NPs to the PVDF-TrFE EFs did not improve the V/N of the impact force sensors (as there is a large overlap in standard deviations of the mean values), however, with hydrothermal growth of the ZnO NPs into ZnO NWs the V/N very clearly statistically significantly increased for all four ZnONWs@PVDF-TrFE samples compared to the samples without ZnO NWs ( $p$ -value < 0.001). This displays a similar trend to results found in other literature regarding the enhancement of impact force piezoelectric output of PVDF materials with incorporated ZnO nanomaterials.<sup>[30,61]</sup>

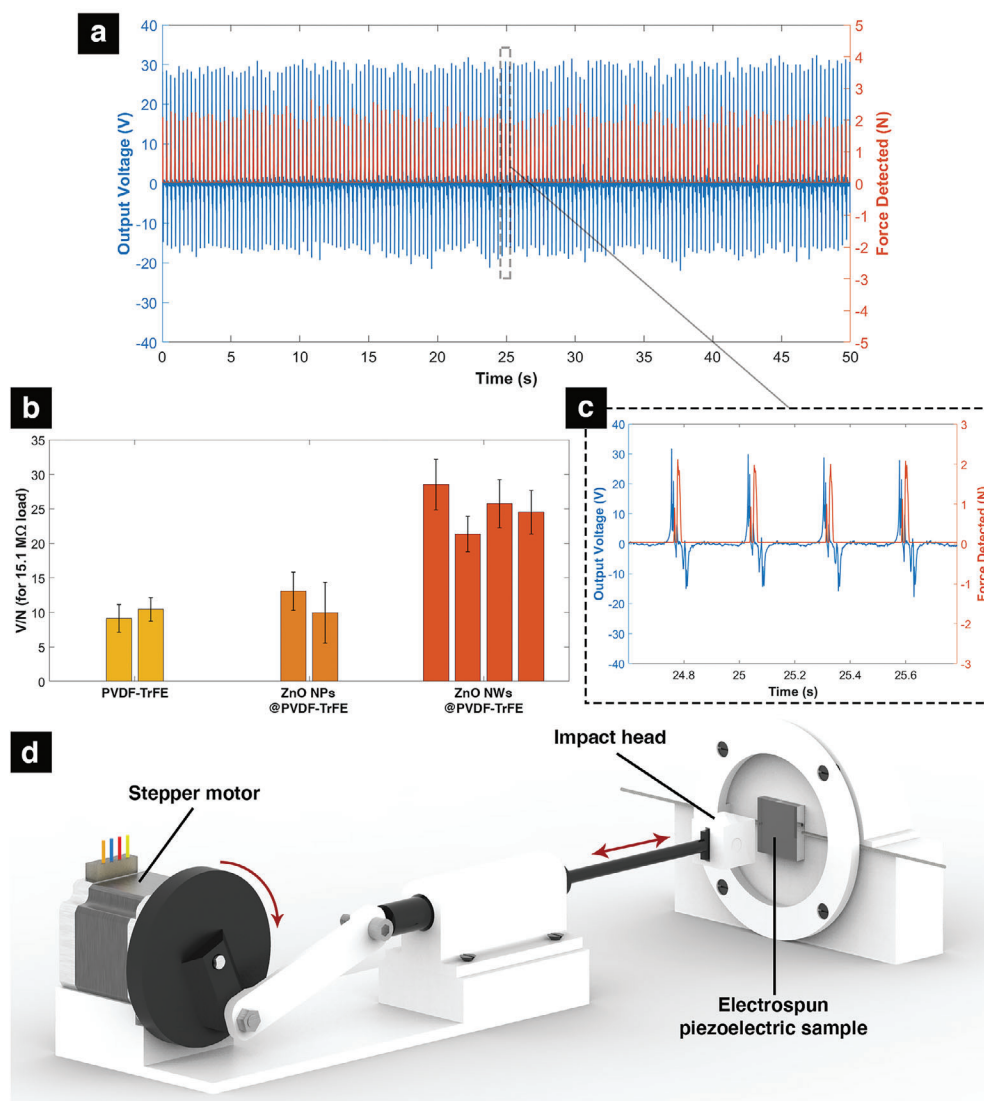


**Figure 5.** Consistent horizontal impact force testing with a) example peak-to-peak voltage and measured force output from a ZnO NW @ PVDF-TrFE piezoelectric sample with a 15.1 MΩ load; b) comparison of output voltage per Newton of applied force (V/N) of PVDF-TrFE, ZnONPs@PVDF-TrFE, and ZnONWs@PVDF-TrFE piezoelectric samples with a 15.1 MΩ load; c) magnified example output signal of four actuations taken from (a); and d) rendered image of the 3D-printed linear actuator.

The signal drift of each output signal was also measured by comparing the difference between the average  $V_{pp}$  of the first and final 10 impacts. It was found that the signals drifted by an average of  $9.0 \pm 1.8\%$ ,  $4.1 \pm 2.7\%$ , and  $5.0 \pm 2.6\%$  for PVDF-TrFE, ZnONPs@PVDF-TrFE, and ZnONWs@PVDF-TrFE EF samples, respectively. These results indicate a high level of stability of piezoelectric performance with repeated impacts for all three groups, while the ZnO-modified samples demonstrated around half the signal drift of the unmodified samples.

While the 3D-printed horizontal linear actuator provided a good comparison of the three different types of electrospun piezoelectric impact sensor by utilizing consistent impact forces, the applied forces were relatively low and did not provide an adequate range of forces to investigate the linearity of the impact sensor response. To test this, another homebuilt setup was utilized,

which is displayed in Figure 6c. A 2 m long polycarbonate tube (40 mm outer diameter; 36 mm inner diameter) was attached to a wooden structure (C16 whitewood timber) using 3D-printed clamps. A 3D-printed hollow tube, with a PDMS stopper casted to the bottom (Figure 6c inset), was then dropped through the tube onto an electrospun piezoelectric impact sensor positioned at the bottom, which was connected to an oscilloscope to measure the output voltage (with a 1 MΩ load input from the oscilloscope). To alter the mass of the 3D-printed tube, 12 g lead weights were inserted and held using a PDMS stopper. This provided a range of masses between 25 and 570 g that could be dropped onto the impact sensors.

Figure 6a displays an example voltage output from a ZnONWs@PVDF-TrFE EF piezoelectric impact sensor with a dropped mass of 206 g. The initial impact can be seen with the

**Table 2.** Electrospun piezoelectric impact sensor data for horizontal and vertical (drop) impact tests.

	Electrospun piezoelectric impact sensor component		
	PVDF-TrFE	ZnONPs@PVDF-TrFE	ZnONWs@PVDF-TrFE
Horizontal impact			
Number of sensors tested	2	2	4
Average impact force (N) for:			
1.6 M $\Omega$ load	$2.8 \pm 0.3$	$2.7 \pm 0.8$	$2.3 \pm 0.7$
15.1 M $\Omega$ load	$3.2 \pm 1.4$	$2.8 \pm 1.4$	$2.6 \pm 0.7$
Average V/N with impacts at $f = 3.6$ Hz (V/N) for:			
1.6 M $\Omega$ load	$1.6 \pm 0.4$	$2.2 \pm 0.9$	$3.4 \pm 0.6$
15.1 M $\Omega$ load	$9.8 \pm 2.2$	$11.5 \pm 5.1$	$25.0 \pm 3.5$
Vertical (drop) impact			
Tested linear range [N]	117–970	90–858	105–844
Load [M $\Omega$ ]	1	1	1
Sensitivity–impact force [mV N $^{-1}$ ]	11.0	30.8	63.9
Sensitivity–impact energy [V J $^{-1}$ ]	0.98	2.20	4.25
R $^2$	0.971	0.951	0.986

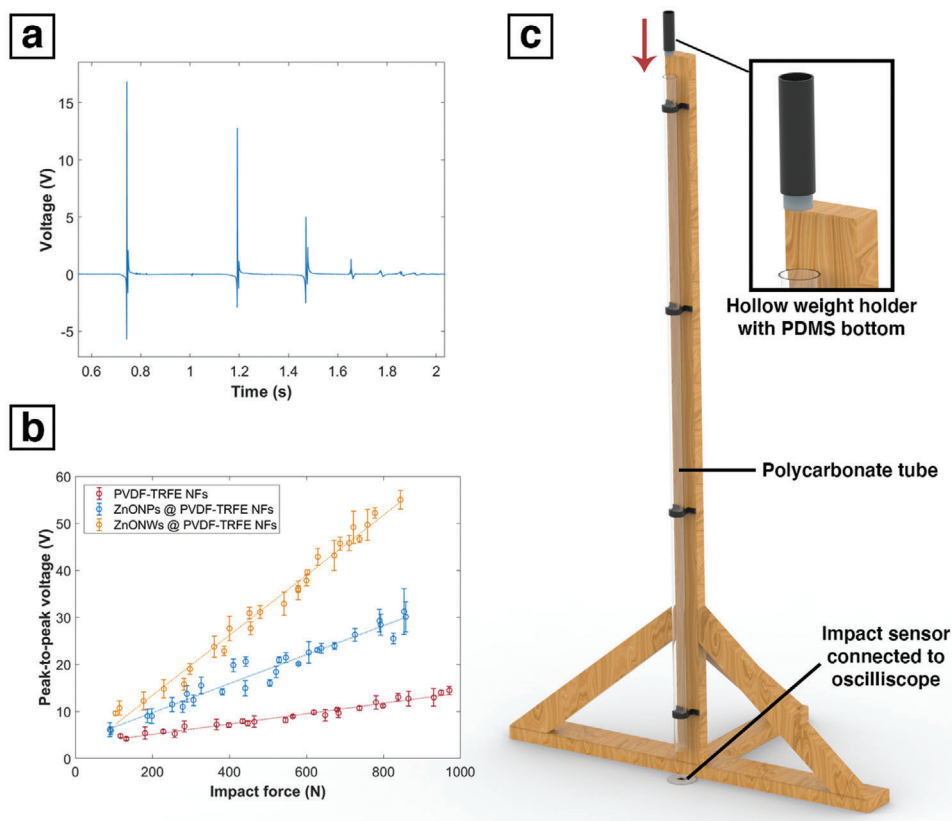


**Figure 6.** Vertical drop impact testing of electrospun piezoelectric impact sensors with a) example drop impact test output signal of ZnONWs@PVDF-TrFE EFs with a mass of 206 g; b) output  $V_{pp}$  versus impact force for PVDF-TrFE, ZnONPs@PVDF-TrFE, and ZnONWs@PVDF-TrFE EF impact sensors; and c) render of home-built vertical drop impact testing setup.

first peak, followed by several decreasing peaks from the subsequent bounces. The  $V_{pp}$  of the first impact was collected for each dropped mass (repeated three times and averaged). The theoretical impact force ( $F_{theory}$ ) was calculated using Equation (4), with the time of impact ( $t_{impact}$ ) calculated using the FDHM of the absolute value of the first impact  $V_{pp}$  signal (more details found in Section S2, Supporting Information). The velocities of the mass before and after impact ( $v_{int}$  and  $v_{fin}$ , respectively) were calculated theoretically using Equation (3). The impact forces calculated using theoretical  $v_{int}$  and  $v_{fin}$  values ( $F_{theory}$ ) were compared to the impact forces calculated using the experimentally measured  $v_{int}$  and  $v_{fin}$  ( $F_{exp}$ ) in Figure S8 (, Supporting Information), where it was found that the results fit the theoretical model well ( $R^2 = 0.943$ ). Hence,  $F_{theory}$  was used for piezoelectric impact sensor comparison for simplicity.

The output  $V_{pp}$  versus the applied impact force was plotted for PVDF-TrFE, ZnONPs@PVDF-TrFE, and ZnONWs@PVDF-TrFE EF piezoelectric impact sensors (Figure 6b). From this it can be seen that the PVDF-TrFE EFs, with no added ZnO nanomaterials, provided the lowest sensitivity across the tested impact forces ( $11.0 \text{ mV N}^{-1}$ ). The attachment of ZnO NPs to PDA/PVDF-TrFE EFs saw an increase in sensitivity to  $30.8 \text{ mV N}^{-1}$ , while the growth into ZnO NWs gave the highest sensitivity with  $63.9 \text{ mV N}^{-1}$ . For each sensor, the responses were linear with a high goodness of fit in each case ( $R^2 = 0.971, 0.951$ , and  $0.986$  for PVDF-TrFE, ZnONPs@PVDF-TrFE, and ZnONWs@PVDF-TrFE EFs, respectively). The main results from horizontal and vertical (drop) impact testing can be found in Table 2.

There are several points to note from the data in Figures 5b and 6b, and Table 2. First, while the average impact force remained fairly consistent ( $SD = \pm 1.0 \text{ N}$ ) across all the horizontal impact tests, it can be seen that the V/N coefficient of variation for the ZnONPs@PVDF-TrFE EF sensors was around double that of the PVDF-TrFE sensor and triple the ZnONWs@PVDF-TrFE EF sensor value (22.4%, 44.3%, and 14.0% coefficients of variation for PVDF-TrFE, ZnONPs@PVDF-TrFE, and ZnONWs@PVDF-TrFE EF sensors, respectively, for a  $15.1 \text{ M}\Omega$  load. 25.0%, 40.9%, and 17.6% for same respective coefficient of variations for a  $1.6 \text{ M}\Omega$  load). This may be explained by the efficient electron transfer of ZnO and the electrospun sensors' differing abilities at providing new electron transfer pathways when deformed. For example, when ZnO nanomaterials contact each other during the compression experienced due to an impact, a new conductive pathway will be formed. For attached ZnO NWs, these contacts will be more likely, more numerous, and with a higher contact area. However, due to the smaller surface area of ZnO NPs, these contact points during impact will be less consistent, leading to higher standard deviations.<sup>[26]</sup> Therefore, it can be seen that the hydrothermal growth of ZnO NPs into ZnO NWs not only increases the output voltage but also improves the reproducibility.

The impact force sensing performance of the ZnONWs@PVDF-TrFE EF sensors in this study was compared to other similar studies in research literature. Kim et al. prepared PVDF EFs and hydrothermally grew ZnO NWs on their fibers using three rounds of immersion and curing in a seed solution.<sup>[32]</sup> For a load of  $15 \text{ M}\Omega$  and repeated impacts of pressure  $100 \text{ kPa}$ , with a frequency of  $1 \text{ Hz}$ , the average  $V_{pp}$  of their ZnO/PVDF EFs was found to be  $1.9 \text{ V}$ . Meanwhile, in

this study, the average  $V_{pp}$  for the same load and lower impact pressure ( $10.0 \pm 3.8 \text{ kPa}$ ) was measured as  $61.2 \pm 15.8 \text{ V}$ . An explanation for this much larger output voltage could be due to the use of PVDF-TrFE instead of PVDF, which has been shown to crystallize with a greater proportion of  $\beta$ -phase crystallinity, or could also be a result of the addition of PDA as an electron transfer layer before the ZnO attachment. To reinforce the latter point, Yang et al. argued that, without the addition of a PDA layer, inorganic nanomaterials will only have a loose contact with organic polymers, which results in a large number of hole defects and cracks.<sup>[15]</sup> This leads to piezoelectric-induced charges accumulating at defect sites, which act as electron traps, and detrimentally effects the sensor performance. Similarly, the ZnONWs@PVDF-TrFE EF impact sensors in this paper also showed sensitivity improvements over sensors using nano-ZnO/PVDF-TrFE thin films<sup>[30]</sup> and ZnONWs/conductive fabric/PVDF EFs<sup>[33]</sup> as well as PVDF EF sensors with BTO/PDA NPs.<sup>[15]</sup> These comparisons can be found in Table 3.

From these results, it can be seen that the ZnONWs@PVDF-TrFE EFs offer a V/N piezoelectric output that is suitable for wearable sensing applications and energy harvesting.

### 3.3. Wearable Sensing of Soccer Ball Heading Impact Force

Heading a soccer ball is an important and commonly used skill in association football, with the average professional player estimated to conduct six headers in a 90 min match, or  $\approx 2000$  in a 300-match career, disregarding practice sessions.<sup>[96,97]</sup> For smaller impact headers (e.g., a headed short range pass) the impact force has been shown to be within safe levels (for a ball speed of  $2\text{--}3 \text{ m s}^{-1}$ , impact force was  $\approx 100 \text{ N}$ ).<sup>[97]</sup> However, for higher impact headers (e.g., heading a ball while defending a direct free kick, which can reach horizontal speeds of around  $28\text{--}34 \text{ m s}^{-1}$ ), the head may experience impact forces of over  $1 \text{ kN}$ .<sup>[98]</sup> It is important to note that the impact force that a soccer ball may exert on the head of a player is not enough to predict potential health hazards (such as a concussion) on its own as many factors must be taken into account when considering the dangers of a particular impact force, such as the neck strength of the participant or acceleration of the head after impact. Nevertheless, such high, numerous impacts to the head sustained over a career of 10–20 years have recently been strongly linked to causing neurodegenerative diseases in the later lives of professional soccer players.<sup>[99]</sup>

It is therefore useful to have a soft flexible impact sensor, capable of measuring a large range of forces, which can be incorporated into soccer players' headwear in an unobtrusive manner to monitor soccer ball heading impact forces. To investigate the potential of the ZnONWs@PVDF-TrFE EF piezoelectric impact sensors for this application, one of the sensors was incorporated into an elastic headband to be worn while heading a soccer ball (Figure 7b). A professional grade soccer ball (size 5,  $0.81 \text{ bar}$ ), with a mass of  $426 \text{ g}$ , was dropped from a height of  $2 \text{ m}$  above the head of a subject wearing the headband impact sensor (Figure 7a).

The output voltage was recorded using an oscilloscope for three impacts and the impact force ( $F_{sensor}$ ) was calculated using the calibration equation found from the vertical drop calibration



**Table 3.** Comparison of piezoelectric impact sensing data from this study and others.

	ZnONWs/PVDF EFs <sup>[32]</sup>	ZnONWs/conductive fabric/PVDF EFs <sup>[33]</sup>	Nano-ZnO/PVDF-TrFE thin film <sup>[30]</sup>	BTO/PDA NPs @ PVDF thin film <sup>[15]</sup>
Load	15 M $\Omega$	Open circuit	Not specified	1 M $\Omega$
Linear range	100 kPa only	3–150 kPa	0–359 mJ	12–243 N
Impact sensitivity	18.9 mV kPa <sup>-1</sup>	11.1 mV kPa <sup>-1</sup>	0.735 V J <sup>-1</sup>	4.3 mV N <sup>-1</sup>
Impact sensitivity—This work	6060.6 mV kPa <sup>-1</sup>	39.4 mV kPa <sup>-1</sup> (1 M $\Omega$ load)	4.250 V J <sup>-1</sup> (1 M $\Omega$ load)	63.9 mV N <sup>-1</sup>

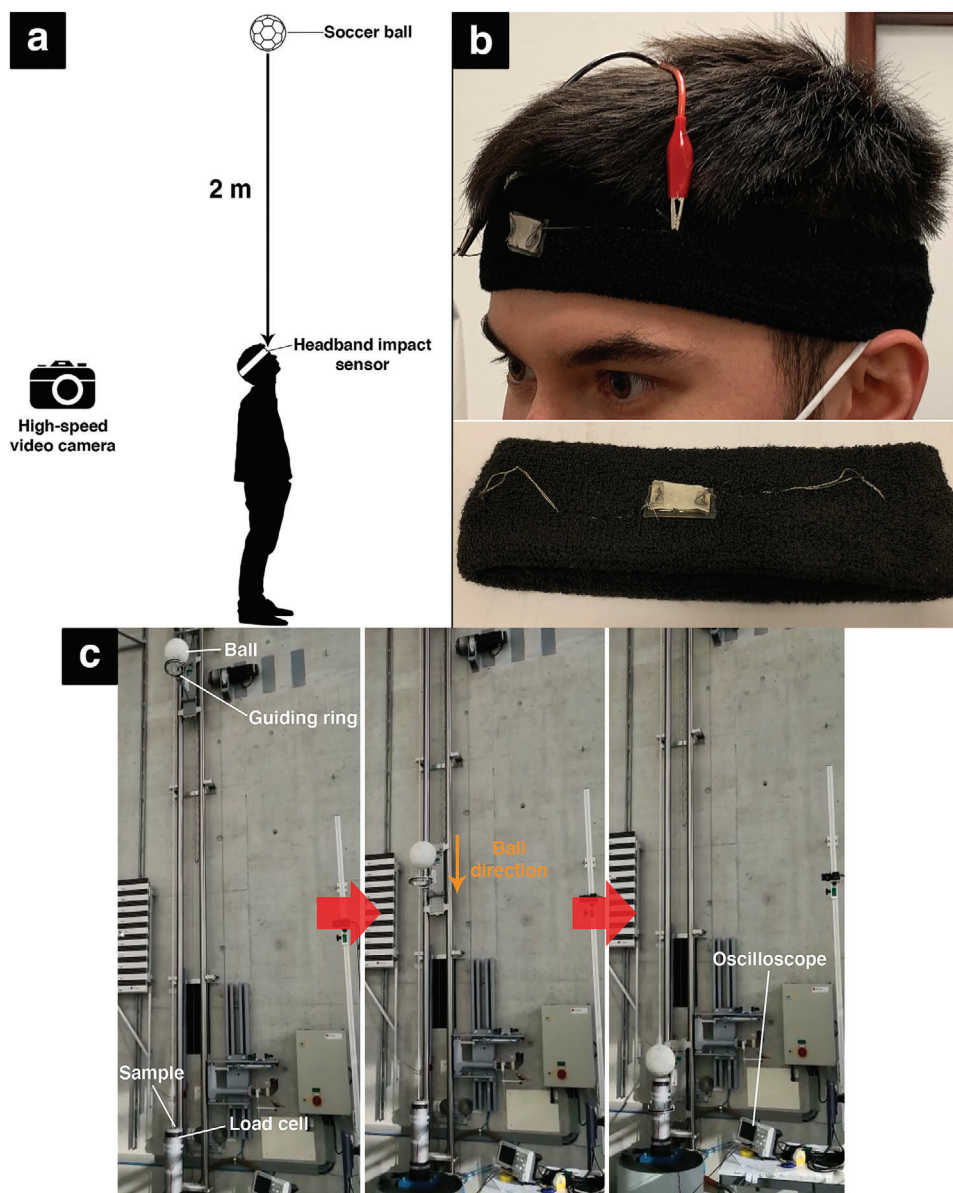


**Figure 7.** Equipment to measure impact force from dropped soccer ball with a) schematic of experimental set up for soccer ball impact force detection on the head; b) ZnONWs@PVDF-TrFE EF impact sensor integrated into a wearable headband and connected to oscilloscope; and c) FIFA-accredited free fall setup used to recalibrate the wearable impact sensor with a soccer ball.

**Table 4.** Soccer ball impact force during data.

No.	$V_{pp}$ [V]	$t_{\text{contact}}$ [ms]	$F_{\text{theory}}$ [N]	$F_{\text{exp}}$ [N]	$F_{\text{sensor 1}}$ [N]	$F_{\text{sensor 2}}$ [N]	Error between $F_{\text{sensor}}$ and $F_{\text{theory}}/F_{\text{exp}}$ [%]	
							$F_{\text{sensor 1}}$	$F_{\text{sensor 2}}$
1	15.87	14.2	382.0	381.9	238.9	362.7	−37.4 / −37.4	−5.0 / −5.0
2	22.38	8.7	597.1	562.3	340.8	514.8	−42.9 / −39.4	−13.8 / −8.4
3	19.41	11.7	461.8	483.5	294.4	445.4	−36.3 / −39.1	−3.5 / −7.9

Note:  $F_{\text{sensor 1}}$  = calibrated with home-built setup;  $F_{\text{sensor 2}}$  = calibrated with FIFA-accredited setup.

testing. Table 4 details the impact forces calculated theoretically ( $F_{\text{theory}}$ ) and experimentally using a high-speed camera ( $F_{\text{exp}}$ ), as well as comparing  $F_{\text{sensor}}$  to these values. It can be observed that all impact forces measured by the sensor were lower than the calculated impact forces, with large errors ranging between 36.3% and 42.9%. The consistent large errors could be caused by a number of factors such as the accuracy and consistency of the calibration process, the impact area of the dropped mass, and the difference in the softness between the material of the soccer ball and the material of the mass used to calibrate the impact sensor. Softer materials have a higher  $t_{\text{contact}}$  during impact than harder materials, leading to lower impact forces experienced. Furthermore, while samples were calibrated on a rigid hard surface, wearable soccer ball impact detection will be influenced by the soft and viscoelastic nature of the human skin and the wearable headband material.

Hence, to improve the accuracy of the wearable impact sensor, the ZnONWs@PVDF-TrFE EF sample was recalibrated using a FIFA-accredited free fall system (Figure 6c), which enables highly precise and repeatable soccer ball impact force measurements.<sup>[76]</sup> A new calibration curve was calculated by accurately guiding a falling soccer ball onto the sensor from heights ranging between 1 and 4 m and measuring the resulting impact force with an integrated load cell (Figure S11, Supporting Information). This was used to recalculate the detected forces found using the wearable headband sensor and, from the results in Table 4, a large reduction in error between measured and calculated impact forces was observed. This highlights the importance of material choice and size during calibration. Any remaining error will likely be a consequence of uneven morphology of the impact surface on the head and components of the impact force acting along the horizontal axis (the heading impacts will never be perfectly vertical).

From this study, the average velocity of the soccer ball just before impact was measured as  $7.8 \pm 1.5 \text{ m s}^{-1}$  and the average impact force experienced was  $441.0 \pm 76.1 \text{ N}$ . This is around half the value of the peak soccer ball free fall impact forces measured in a study conducted by Levendusky et al.<sup>[100]</sup> (912 N) with a falling velocity of  $18 \text{ m s}^{-1}$ . This force value is also below the estimated threshold for potential damage or concussion caused by repeated impacts ( $>784 \text{ N}$ ),<sup>[97]</sup> however, the ball velocity measured in this study was only  $\approx 25\%$  of the potential maximum velocity.<sup>[98]</sup> Hence, for future studies, faster ball velocities will be considered to recreate higher head impact forces that will be experienced during professional soccer matches.

From these results, it can be concluded that the ZnONWs@PVDF-TrFE EFs have potential to be incorporated into sensitive wearable impact force sensors.

## 4. Conclusion

In this work, PVDF-TrFE fibers were fabricated using high-throughput, nozzle-free electrospinning and coated with a self-polymerized PDA layer to facilitate strong attachment of ZnO NPs. These ZnO NPs were hydrothermally grown into ZnO NWs before the piezoelectric voltage output was compared for PVDF-TrFE, ZnONPs@PVDF-TrFE, and ZnONWs@PVDF-TrFE EFs using two different low-cost, home-built impact force testing setups.

It was found that, by attaching ZnO NWs to the PVDF-TrFE EFs, the piezoelectric impact force sensor sensitivity increased to  $25.0 \pm 3.5 \text{ V N}^{-1}$  compared to  $9.8 \pm 2.2 \text{ V N}^{-1}$  of the unmodified PVDF-TrFE EFs (2.55-fold increase), using horizontal impact tests of  $2.6 \pm 1.0 \text{ N}$  at 3.6 Hz with a  $15.1 \text{ M}\Omega$  load. Similarly, using vertical drop impact testing demonstrated an increase from  $11.0$  to  $63.9 \text{ mV N}^{-1}$  in sensitivity (5.80-fold increase) with a linear response ( $R^2 = 0.986$ ) for a large range of impact forces up to  $970 \text{ N}$  (load =  $1 \text{ M}\Omega$ ). Comparing the impact force sensitivity values of the ZnONWs@PVDF-TrFE EFs in this work to similar studies utilizing PVDF and ZnO in other research literature highlighted a clear improvement in piezoelectric voltage output. This was believed to be due to a combination of the higher proportion of polar  $\beta$ -phase crystallinity in PVDF-TrFE EFs compared to pure PVDF (confirmed by XRD and ATR-FTIR data) and the coating of a thin PDA layer which acts as an electron transfer layer and robust anchoring site between organic and inorganic materials. The robust attachment was confirmed with SEM images showing homogeneously-grown and attached ZnO NWs to PDA-coated PVDF-TrFE EFs after 40 min total ultrasonication, while the ZnO NWs were sparsely attached on uncoated PVDF-TrFE EFs after the same period of ultrasonication.

The ZnONWs@PVDF-TrFE EF impact force sensors were also integrated into a wearable headband for soccer ball head impact sensing. Here, with initial calibration, it was measured that the average vertical drop impact force of a soccer ball on the head of a human male participant was  $291.4 \pm 51.0 \text{ N}$  for a ball speed of  $7.8 \pm 1.5 \text{ m s}^{-1}$ . This sensor-measured impact force had a large average  $-38.6 \pm 1.1\%$  error compared to the impact forces calculated from high-speed camera footage. Through recalibration of the sensor with a FIFA-accredited guided free fall setup using a soccer ball, the sensor-measured average impact force was recalculated as  $441.0 \pm 76.1 \text{ N}$ , with an improved error of  $-7.1 \pm 1.8\%$ . This highlighted the importance of material choice of the mass during sensor calibration.

From these results, it was concluded that the ZnONWs@PVDF-TrFE EFs would be suitable for wearable

impact force applications, in fields such as sports monitoring, as well as for wearable energy harvesting.

## Supporting Information

Supporting Information is available from the Wiley Online Library or from the author.

## Acknowledgements

This work was supported by the EPSRC CDT in Intelligent Sensing and Measurement, grant number EP/L016753/1. The authors would like to thank the following people: Dr. Gary Nicol for assistance with XRD measurements; Dr. Andrea Arcifa for assistance with XPS measurements; Owen Anderson for assembling the home-built vertical impact testing setup; and Natalie Chung and Gregor McFarlane for their assistance with soccer ball heading impact force experiments.

## Conflict of Interest

The authors declare no conflict of interest.

## Author Contributions

M.C. conceptualized the work, authored the first draft of the paper and made subsequent edits. F.J.D.S. electrospun the PVDF-TrFE/PEO EFs, conducted horizontal impact force experiments, and assisted with assembly of electrospun impact sensors as well as soccer ball head impact tests. J.S. conducted XPS/ATR-FTIR measurements and assisted with XPS analysis. All other experiments and data analyses were conducted by M.C. N.R. assisted with writing and provided feedback as well as supervision.

## Data Availability Statement

The data that support the findings of this study are available from the corresponding author upon reasonable request.

## Keywords

electrospinning, impact force, nanomaterials, piezoelectrics, polydopamine, PVDF-TrFE, soccer ball impact, wearable sensors, zinc oxide

Received: November 11, 2022  
Revised: December 28, 2022  
Published online: January 18, 2023

- [1] Y. Yang, W. Gao, *Chem. Soc. Rev.* **2018**, *48*, 1465.
- [2] S. Nasiri, M. R. Khosravani, *Sens. Actuators, A* **2020**, *312*, 112105.
- [3] M. Rana, V. Mittal, *IEEE Sens. J.* **2021**, *21*, 1187.
- [4] M. Chung, G. Fortunato, N. Radacsi, *J. R. Soc., Interface* **2019**, *16*, 20190217.
- [5] D. R. Seshadri, R. T. Li, J. E. Voos, J. R. Rowbottom, C. M. Alfes, C. A. Zorman, C. K. Drummond, *npj Digital Med.* **2019**, *2*, 72.
- [6] Y. Song, D. Mukasa, H. Zhang, W. Gao, *Acc. Mater. Res.* **2021**, *2*, 184.
- [7] J. Kim, A. S. Campbell, J. Wang, *Talanta* **2018**, *177*, 163.

- [8] H. Teymourian, A. Barfidokht, J. Wang, *Chem. Soc. Rev.* **2020**, *49*, 7671.
- [9] Y. Fang, Y. Zou, J. Xu, G. Chen, Y. Zhou, W. Deng, X. Zhao, M. Rous-taei, T. K. Hsiai, J. Chen, *Adv. Mater.* **2021**, *33*, 2104178.
- [10] Y. Peng, J. Zhou, X. Song, K. Pang, A. Samy, Z. Hao, J. Wang, *Sensors* **2021**, *21*, 485.
- [11] S. Chen, N. Wu, S. Lin, J. Duan, Z. Xu, Y. Pan, H. Zhang, Z. Xu, L. Huang, B. Hu, J. Zhou, *Nano Energy* **2020**, *70*, 104460.
- [12] K.-Y. Shin, J. S. Lee, J. Jang, *Nano Energy* **2016**, *22*, 95.
- [13] D. R. Seshadri, E. V. Davies, E. R. Harlow, J. J. Hsu, S. C. Knighton, T. A. Walker, J. E. Voos, C. K. Drummond, *Front. Digital Heal.* **2020**, *2*, 8.
- [14] S. Ma, T. Ye, T. Zhang, Z. Wang, K. Li, M. Chen, J. Zhang, Z. Wang, S. Ramakrishna, L. Wei, *Adv. Mater. Technol.* **2018**, *3*, 1800033.
- [15] Y. Yang, H. Pan, G. Xie, Y. Jiang, C. Chen, Y. Su, Y. Wang, H. Tai, *Sens. Actuators, A* **2020**, *301*, 111789.
- [16] G.-Y. Li, J. Li, Z.-J. Li, Y.-P. Zhang, X. Zhang, Z.-J. Wang, W.-P. Han, B. Sun, Y.-Z. Long, H.-D. Zhang, *Adv. Compos. Hybrid Mater.* **2021**, *5*, 766.
- [17] C. Xu, Y. Yang, W. Gao, *Matter* **2020**, *2*, 1414.
- [18] Y. Liu, J. J. S. Norton, R. Qazi, Z. Zou, K. R. Ammann, H. Liu, L. Yan, P. L. Tran, K.-I. Jang, J. W. Lee, D. Zhang, K. A. Kilian, S. H. Jung, T. Bretl, J. Xiao, M. J. Slepian, Y. Huang, J.-W. Jeong, J. A. Rogers, *Sci. Adv.* **2016**, *2*, e1601185.
- [19] P. Fontana, N. R. A. Martins, M. Camenzind, R. M. Rossi, F. Baty, M. Boesch, O. D. Schoch, M. H. Brutsche, S. Annaheim, *Sensors* **2019**, *19*, 2436.
- [20] G. Chen, Y. Li, M. Bick, J. Chen, *Chem. Rev.* **2020**, *120*, 3668.
- [21] D. H. Kang, N. K. Kim, H. W. Kang, *Nanotechnology* **2019**, *30*, 365303.
- [22] J. D. Ryan, A. Lund, A. I. Hofmann, R. Kroon, R. Sarabia-Riquelme, M. C. Weisenberger, C. Müller, *ACS Appl. Energy Mater.* **2018**, *1*, 2934.
- [23] T. Sun, B. Zhou, Q. Zheng, L. Wang, W. Jiang, G. J. Snyder, *Nat. Commun.* **2020**, *11*, 572.
- [24] Y.-E. Shin, J.-E. Lee, Y. Park, S.-H. Hwang, H. G. Chae, H. Ko, *J. Mater. Chem. A* **2018**, *6*, 22879.
- [25] W. Seung, M. K. Gupta, K. Y. Lee, K. Shin, J. Lee, T. Y. Kim, S. Kim, J. Lin, J. H. Kim, S. Kim, *ACS Nano* **2015**, *9*, 3501.
- [26] S. Chen, Z. Lou, D. i Chen, Z. Chen, K. Jiang, G. Shen, *Sci. China Mater.* **2016**, *59*, 173.
- [27] H. Khan, A. Razmjou, M. E. Warkiani, A. Kottapalli, M. Asadnia, *Sensors* **2018**, *18*, 418.
- [28] X. Wang, F. Sun, G. Yin, Y. Wang, B. Liu, M. Dong, *Sensors* **2018**, *18*, 330.
- [29] J. Li, S. Chen, W. Liu, R. Fu, S. Tu, Y. Zhao, L. Dong, B. Yan, Y. Gu, *J. Phys. Chem. C* **2019**, *123*, 11378.
- [30] J. Han, D. Li, C. Zhao, X. Wang, J. Li, X. Wu, *Sensors* **2019**, *19*, 830.
- [31] J. S. Dodds, F. N. Meyers, K. J. Loh, *Sens. Smart Struct. Technol. Civil, Mech. Aerosp. Syst. 2012* **2012**, *8345*, 834515.
- [32] M. Kim, Y. Wu, E. Kan, J. Fan, *Polymers* **2018**, *10*, 745.
- [33] W. Feng, Y. Chen, W. Wang, D. Yu, *Colloids Surf., A* **2021**, *633*, 127890.
- [34] Y. R. Wang, J. M. Zheng, G. Y. Ren, P. H. Zhang, C. Xu, *Smart Mater. Struct.* **2011**, *20*, 045009.
- [35] P. K. Panda, B. Sahoo, *Ferroelectrics* **2015**, *474*, 128.
- [36] A. Jain, K. J. Prashanth, A. K. Sharma, A. Jain, Rashmi PN, *Polym. Eng. Sci.* **2015**, *55*, 1589.
- [37] S. Sukumaran, S. Chatbourni, D. Rouxel, E. Tisserand, F. Thiebaud, T. Ben Zineb, *J. Intell. Mater. Syst. Struct.* **2021**, *32*, 746.
- [38] N. Shehata, A. H. Hassanin, E. Elnabawy, R. Nair, S. A. Bhat, I. Kand-das, *Sensors* **2020**, *20*, 3111.
- [39] E. Cho, C. Kim, J.-K. Kook, Y. I. Jeong, J. H. Kim, Y. A. Kim, M. Endo, C. H. Hwang, *J. Membr. Sci.* **2012**, *389*, 349.



- [40] P. Thakur, A. Kool, N. A. Hoque, B. Bagchi, F. Khatun, P. Biswas, D. Brahma, S. Roy, S. Banerjee, S. Das, *Nano Energy* **2018**, *44*, 456.
- [41] T. Nishiyama, T. Sumihara, Y. Sasaki, E. Sato, M. Yamato, H. Horibe, *Polym. J.* **2016**, *48*, 1035.
- [42] K. Gao, X. Hu, C. Dai, T. Yi, *Mater. Sci. Eng., B* **2006**, *131*, 100.
- [43] P. Saxena, P. Shukla, *Adv. Compos. Hybrid Mater.* **2021**, *4*, 8.
- [44] S. P. Bao, G. D. Liang, S. C. Tjong, *Carbon* **2011**, *49*, 1758.
- [45] M. Baniasadi, Z. Xu, J. Cai, S. Daryadel, M. Quevedo-Lopez, M. Naraghi, M. Minary-Jolandan, *Polymer* **2017**, *127*, 192.
- [46] D. K. Das-Gupta, K. Doughty, *J. Appl. Phys.* **1978**, *49*, 4601.
- [47] G. Ren, F. Cai, B. Li, J. Zheng, C. Xu, *Macromol. Mater. Eng.* **2013**, *298*, 541.
- [48] A. Keirouz, M. Chung, J. Kwon, G. Fortunato, N. Radacsi, *Wiley Interdiscip. Rev.: Nanomed. Nanobiotechnol.* **2020**, *12*, e1626.
- [49] M. Chung, W. H. Skinner, C. Robert, C. J. Campbell, R. M. Rossi, V. Koutsos, N. Radacsi, *ACS Appl. Mater. Interfaces* **2021**, *13*, 51504.
- [50] D. H. Reneker, A. L. Yarin, *Polymer* **2008**, *49*, 2387.
- [51] G. Kalimuldina, N. Turdakyn, I. Abay, A. Medeubayev, A. Nurpeissova, D. Adair, Z. Bakenov, *Sensors* **2020**, *20*, 5214.
- [52] A. K. Maurya, E. Mias, J. Schoeller, I. E. Collings, R. M. Rossi, A. Dommann, A. Neels, *Nanoscale Adv.* **2022**, *4*, 491.
- [53] S. Goel, B. Kumar, *J. Alloys Compd.* **2020**, *816*, 152491.
- [54] A. T. Le, M. Ahmadipour, S.-Y. Pung, *J. Alloys Compd.* **2020**, *844*, 156172.
- [55] N. Ahmad, X. Zhang, S. Yang, D. Zhang, J. Wang, S. U. Zafar, Y. Li, Y. Zhang, S. Hussain, Z. Cheng, A. Kumaresan, H. Zhou, *J. Mater. Chem. C* **2019**, *7*, 10795.
- [56] J. H. Kim, M. K. Joshi, J. Lee, C. H. Park, C. S. Kim, *J. Colloid Interface Sci.* **2018**, *513*, 566.
- [57] H. Wu, D. Lin, R. Zhang, W. Pan, *J. Am. Ceram. Soc.* **2008**, *91*, 656.
- [58] M. Liu, Y. Liu, L. Zhou, *Micromachines* **2021**, *12*, 602.
- [59] M. Ahmad, C. Pan, Z. Luo, J. Zhu, *J. Phys. Chem. C* **2020**, *114*, 9308.
- [60] J. Ma, Q. Zhang, K. Lin, L. Zhou, Z. Ni, *Mater. Res. Express* **2018**, *5*, 035057.
- [61] J. Li, C. Zhao, K. Xia, X. Liu, D. Li, J. Han, *Appl. Surf. Sci.* **2019**, *463*, 626.
- [62] V. S. Nguyen, D. Rouxel, B. Vincent, L. Badie, F. D. D. Santos, E. Lamouroux, Y. Fort, *Appl. Surf. Sci.* **2013**, *279*, 204.
- [63] Y. Su, W. Li, L. Yuan, C. Chen, H. Pan, G. Xie, G. Conta, S. Ferrier, X. Zhao, G. Chen, H. Tai, Y. Jiang, J. Chen, *Nano Energy* **2021**, *89*, 106321.
- [64] X. Wang, W. Hu, *CrystEngComm* **2017**, *19*, 6182.
- [65] M. E. Lynge, R. Van Der Westen, A. Postma, B. Städler, *Nanoscale* **2011**, *3*, 4916.
- [66] J. H. Ryu, P. B. Messersmith, H. Lee, *ACS Appl. Mater. Interfaces* **2018**, *10*, 7523.
- [67] F. J. Diaz Sanchez, M. Chung, M. Waqas, V. Koutsos, S. Smith, N. Radacsi, *Nano Energy* **2022**, *98*, 107286.
- [68] M. Waqas, A. Keirouz, M. K. Sanira Putri, F. Fazal, F. J. Diaz Sanchez, D. Ray, V. Koutsos, N. Radacsi, *Med. Eng. Phys.* **2021**, *92*, 80.
- [69] J. H. Kim, M. K. Joshi, J. Lee, C. H. Park, C. S. Kim, *J. Colloid Interface Sci.* **2018**, *513*, 566.
- [70] L. Vayssieres, K. Keis, S.-E. Lindquist, A. Hagfeldt, *J. Phys. Chem. B* **2001**, *105*, 3350.
- [71] A. B. Djuricic, X. Chen, Y. H. Leung, A. M. C. Ng, *J. Mater. Chem.* **2012**, *22*, 6526.
- [72] S. Baruah, J. Dutta, *Sci. Technol. Adv. Mater.* **2009**, *10*, 013001.
- [73] L. Schmidt-Mende, J. L. Macmanus-Driscoll, *Mater. Today* **2007**, *10*, 40.
- [74] D. Polsongkram, P. Chamninok, S. Pukird, L. Chow, O. Lupan, G. Chai, H. Khallaf, S. Park, A. Schulte, *Phys. B* **2008**, *403*, 3713.
- [75] R. Metz, *Sound Vib.* **2007**, *41*, 18.
- [76] R. Stämpfli, P. A. Brühwiler, *Meas. Sci. Technol.* **2009**, *20*, 115102.
- [77] F. Mokhtari, M. Shamshirsaz, M. Latifi, *Polym. Eng. Sci.* **2016**, *56*, 61.
- [78] F. Mokhtari, J. Foroughi, M. Latifi, *Energy Harvesting Properties of Electrospun Nanofibers* IOP, Bristol, UK **2019**.
- [79] N. A. Alshehri, A. R. Lewis, C. Pleydell-Pearce, T. G. G. Maffei, *J. Saudi Chem. Soc.* **2018**, *22*, 538.
- [80] X. Cai, T. Lei, D. Sun, L. Lin, *RSC Adv.* **2017**, *7*, 15382.
- [81] R. Al-Gaashani, S. Radiman, A. R. Daud, N. Tabet, Y. Al-Douri, *Ceram. Int.* **2013**, *39*, 2283.
- [82] A. Arrigoni, L. Brambilla, C. Bertarelli, G. Serra, M. Tommasini, C. Castiglioni, *RSC Adv.* **2020**, *10*, 37779.
- [83] A. Salimi, A. A. Yousefi, *Polym. Test.* **2003**, *22*, 699.
- [84] Z.-L. Cheung, K.-M. Ng, L.-T. Weng, C.-M. Chan, L. Li, *Polymer* **2006**, *47*, 3164.
- [85] L. Weidenbacher, E. Müller, A. G. Guex, M. Zündel, P. Schweizer, V. Marina, C. Adlhart, L. Vejsadová, R. Pauer, E. Spiecker, K. Maniura-Weber, S. J. Ferguson, R. M. Rossi, M. Rottmar, G. Fortunato, *ACS Appl. Mater. Interfaces* **2019**, *11*, 5740.
- [86] Y.-Y. Choi, J. Hong, D.-S. Leem, M. Park, H. Song, T.-H. Sung, K. No, *J. Mater. Chem.* **2011**, *21*, 5057.
- [87] M. A. Vecchio, A. B. Meddeb, M. T. Lanagan, Z. Ounaies, J. R. Shallenberger, *J. Appl. Phys.* **2018**, *124*, 114102.
- [88] P. Kaspar, D. Sobola, K. Částková, A. Knápek, D. Burda, F. Orudzhev, R. Dallaev, P. Tofel, T. Trcka, L. Grmela, Z. Hadas, *Polymers* **2020**, *12*, 2766.
- [89] D. Mandal, K. Müller, K. Henkel, D. Schmeißer, *Appl. Surf. Sci.* **2012**, *261*, 209.
- [90] *Practical Surface Analysis by Auger and X-Ray Photoelectron Spectroscopy* (Eds: D. Briggs, M. P. Seah), Wiley, Chichester, UK **1983**.
- [91] R. A. Zangmeister, T. A. Morris, M. J. Tarlov, *Langmuir* **2013**, *29*, 8619.
- [92] F. Wei, J. Liu, Y.-N. Zhu, X.-S. Wang, C.-Y. Cao, W.-G. Song, *Sci. China Chem.* **2017**, *60*, 1236.
- [93] M. B. Clark, J. A. Gardella, T. M. Schultz, D. G. Patil, L. Salvati, *Anal. Chem.* **1990**, *62*, 949.
- [94] M. C. Biesinger, L. W. M. Lau, A. R. Gerson, R. S. C. Smart, *Appl. Surf. Sci.* **2010**, *257*, 887.
- [95] J. Lee, J. Chung, S. Lim, *Phys. E* **2010**, *42*, 2143.
- [96] A. D. Witof, F. M. Webbe, *Arch. Clin. Neuropsychol.* **2003**, *18*, 397.
- [97] M. Worsey, B. Jones, A. Cervantes, S. Chauvet, D. Thiel, H. Espinosa, *Electron* **2020**, *9*, 834.
- [98] C. F. Babbs, *Sci. World J.* **2001**, *1*, 281.
- [99] E. R. Russell, D. F. Mackay, K. Stewart, J. A. Maclean, J. P. Pell, W. Stewart, *JAMA Neurol.* **2021**, *78*, 1057.
- [100] T. A. Levendusky, C. W. Armstrong, J. S. Eck, J. Jeziorowski, L. Kugler, in *Science and Football (Routledge Revivals) Proc. First World Congress of Science and Football, Liverpool 13–17th April 1987*, St Edmundsbury Press, Suffolk, **2013**, pp. 385–393.